



Tailoring of optical, hydrophobic, and anti-icing properties of Ca–Mg co-doped ZnO thin films via sol–gel method

Faran Baig¹ · Ali Asif¹ · Muhammad Waseem Ashraf¹ · Hafiz Muhammad Fahad¹

Received: 27 August 2020 / Accepted: 22 December 2020 / Published online: 20 January 2021
© The Author(s), under exclusive licence to Springer Science+Business Media, LLC part of Springer Nature 2021

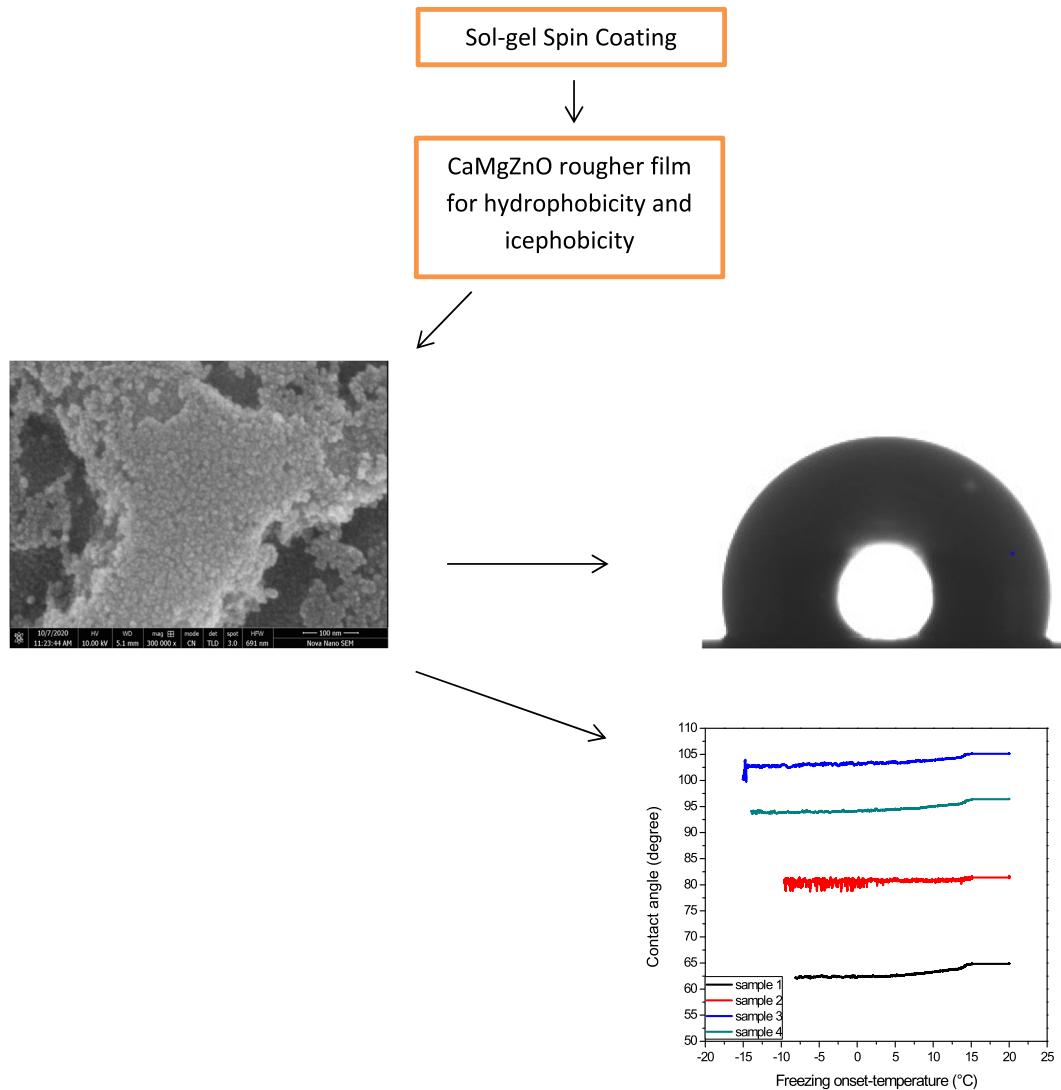
Abstract

Ice formation on solid surfaces may originate serious problems in various fields such as aircraft, electrical lines etc. Hydrophobic coatings and surfaces can have potential applications with anti-icing properties via excessive repellency of water. Zinc oxide (ZnO) is a material with great importance in many technological applications. Recently, co-doping with different elements in zinc oxide is collecting research interest for hydrophobicity. In this work, calcium co-doped with magnesium in zinc oxide (CaMgZnO) thin films were deposited by sol–gel spin coating method. The doping percentage for calcium was $x = 0, 1, 2.5, 4$ at% as $(\text{Ca}_x\text{Mg}_{0.025}\text{Zn}_{0.975-x})$. X-ray diffraction results revealed that all the films had hexagonal wurtzite structure and preferred (002) plane dominance with no secondary phase. Crack free surface was found for all the samples by SEM images. All the deposited films had average transmission of greater than 80%. Maximum band gap value of 3.43 eV revealed for max doping level. Furthermore, optical constants, complex dielectric functions, energy loss functions, and photoluminescence study were also explored. Hydrophobic behavior was evaluated for all the samples and more hydrophobicity with the water contact angle (WCA) of 104.06° produced by the sample having equal amount of calcium and magnesium. De-icing properties like freezing on-set and freezing delay was -15.1°C and 900 s with the temperature set-point -5°C respectively. Likewise, maximum freezing delay with temperature set-point -10°C was 630 s.

✉ Faran Baig
faran_baig@yahoo.com

¹ Department of Physics, GC University, 54000 Lahore, Pakistan

Graphical Abstract



Keywords Zinc oxide · Thin films · Sol–gel · Optical properties · Hydrophobic · Anti-icing

Highlights

- A multifunctional Ca-Mg co-doped ZnO films was prepared by spin-coating method.
- Surface analysis by SEM showed that the morphology was influenced by doping variations.
- The nanostructure provides the Ca-Mg co-doped ZnO films with hydrophobicity and ice-phobicity.
- Optical analysis showed that the transmission of doped ZnO films depends on the doping variation.

1 Introduction

Hydrophobic and anti-icing properties of surfaces with micro or nano-sized topographies have been recently studied [1, 2]. Due to the robust roughness of surfaces, contact area of water to surface efficiently improves the ability to block conductivity of heat or energy from surface to the condensed water droplet [3–5].

In general, doping with appropriate transition metals in semiconductors like zinc oxide (ZnO), is the effective way for applications development. Different dopants may alter various properties of the zinc oxide. Co-doping is famous usually to obtain and improve p-type ZnO [6], n-type ZnO [7], and hydrophobicity of ZnO films [8]. The elements of group II like magnesium and calcium as a dopant can tune the band gap of ZnO [9, 10]. Various methods such as RF

magnetron sputtering [11, 12], chemical spray pyrolysis [13, 14], sol–gel spin coating [15–17], pulse laser deposition [18] etc. have been widely used to synthesize ZnO thin films. In this study, we used sol–gel method because it is simpler and cost effective. Kartikey Verma et al. [19] deposited magnesium doped ZnO films by sol–gel spin coating method and found 3.29 eV maximum band gap. Anca-Ionela Istrate et al. [20] reported different calcium concentrations in zinc oxide with different molarity of the solution in sol–gel method. 0.5 Molarity of the solution offered better transmittance at higher doping level.

Surface on which a droplet of water presents in a spherical shape and have a contact angle greater than 90 degrees is called a hydrophobic surface. The materials with hydrophobic properties are extremely desirable for various applications for example optical devices, micro-fluidic devices, anti-icing coatings, self-cleaning etc. Recently, researchers are studying the wetting properties of various oxides like ZnO [21], TiO₂ [22], Ag₂O [23], and many more. Among all, ZnO is famous for its fascinating properties and applications such as nontoxic nature, high optical transmittance, low electrical resistivity, and abundance in nature. Besides, the hydrophobic and anti-icing properties for ZnO coatings may enlarge its standard electrical and optoelectronic applications domain.

Understanding of ice nucleation on solid surfaces plays an important role for the security of many natural events. The crystallization of ice can be deleterious for many applications like ships, railways, power transmission lines etc. [24–26]. Under extremely low-temperature conditions, the impact of external infrastructure on water to freeze, hence transport facilities causes' serious economic damages and creates human security problems [27–30]. The studies have been completed on ice-phobic and antifreeze materials since 1950s [31–33]. The strategies for submissive ice-phobicity recently attracted attention [34]. The anti-icing (ice-phobicity) properties of materials can improve by contact time to affect supercooled water and ice crystallization delay on the coating surface [35, 36]. The anti-icing (de-icing) is the significant characteristics of surface ice-phobicity and defined as the surface capacity to delay in ice nucleation [37].

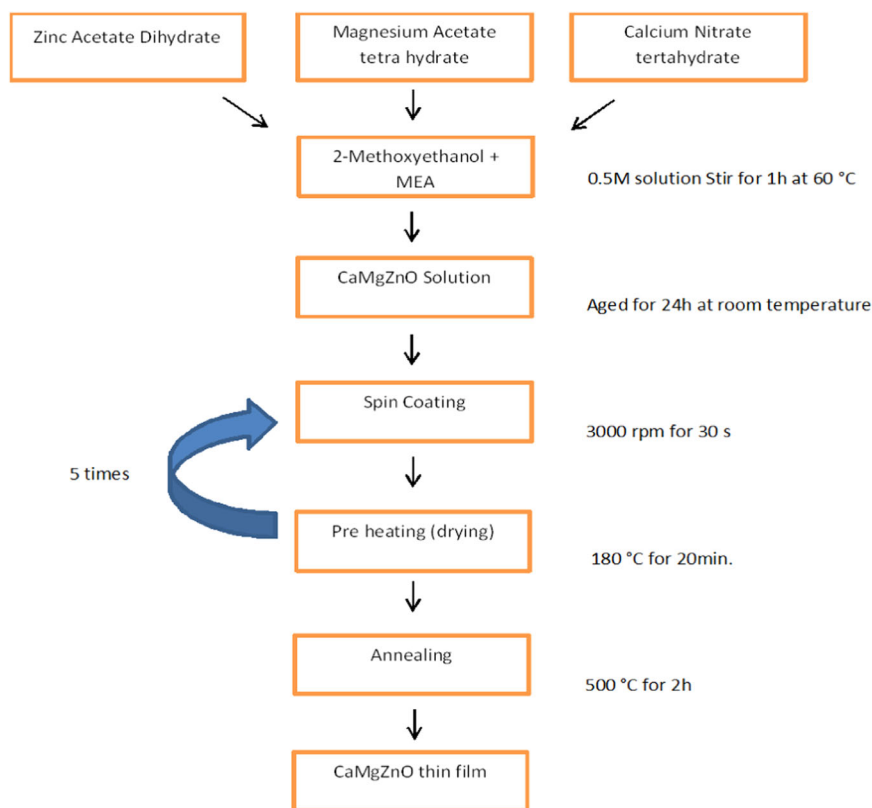
Besides many factors, surface roughness of the coating is the key factor to control ice nucleation process. Many researches have been prepared to prevent water droplet from freezing by enhancing roughness [38–41]. The two classical models that explain wettability of the surface are Cassie–Baxter and Wenzel [42]. The Cassie–Baxter model explains that the water droplet do not completely fix with substrate surface due to less contact area. Therefore this state can better protect the surface from ice formation [42].

This research reported some investigations about hydrophobic and anti-icing properties along with optical results of calcium and magnesium co-doped zinc oxide films. The co-doping has been done due to the reason to obtain uneven surface by ionic radius difference among Ca (0.099 nm), Mg (0.057 nm), and Zn (0.074 nm), to investigate wetting (hydrophobic and hydrophilic), anti-icing and optical properties. The higher doping of magnesium can produce higher band gap with smooth structure but there is a chance of MgO phase to occur [17]. Since calcium doping can produce more band gap enhancement than magnesium but there is a chance of structural distortion by higher ionic radius than Zn. Therefore, by co-doping with low doping percentages may produce higher band gap, less chances of impurity phase and less structural distortion for considerable uneven surface. To the best of our knowledge, a report on the hydrophobic and anti-icing of calcium and magnesium co-doped zinc oxide has not been reported yet. Therefore, high quality and transparent thin films of Ca and Mg co-doped ZnO have been prepared by sol–gel spin coating method. The effects of varied calcium with fix magnesium doping percentage in ZnO on various properties have been explored by XRD, SEM, UV–vis, and OCA (contact angle system) characterization techniques.

2 Experiment

The precursor chemicals include zinc acetate di-hydrate (Zn(CH₃COO)₂·2H₂O), magnesium acetate tetrahydrate (Mg(CH₃COO)₂·4H₂O), and calcium nitrate tetrahydrate (Ca(NO₃)₂·4H₂O). The 2-methoxyethanol and monoethanolamine (MEA) were used as a solvent and stabilizer respectively. The 2-methoxyethanol and MEA reported as the best for surface and optical quality [43]. All the salt chemicals, solvent, and stabilizer were of analytic grade and purchased from Sigma Aldrich. The required quantity of zinc acetate was dissolved in 40 ml of 2-methoxyethanol to prepare 0.5 M solution. After few minutes MEA was added drop by drop to this solution, placed on a magnetic stirrer for 1 h at 60 °C to get a homogeneous solution. An appropriate quantity of 0.5 M sol of magnesium and calcium in 2-methoxyethanol was included to prepare doping percentage for the samples named 1) Ca 0 at%, Mg 2.5 at% in ZnO (Ca_{0.0}Mg_{0.025}Zn_{0.0975}O) (sample 1); 2) Ca 1 at%, Mg 2.5 at% in ZnO (Ca_{0.01}Mg_{0.025}Zn_{0.965}O) (sample 2); 3) Ca 2.5 at%, Mg 2.5 at% in ZnO (Ca_{0.025}Mg_{0.025}Zn_{0.95}O) (sample 3); 4) Ca 4 at%, Mg 2.5 at% in ZnO (Ca_{0.04}Mg_{0.025}Zn_{0.935}O) (sample 4). After the addition of doping percentage, all solutions were further stirred for 30 min. All the solutions were placed at room temperature for aging (24 h). Then the prepared and aged solutions were spin

Fig. 1 Flow diagram of sol–gel spin coating for CaMgZnO thin film



coated on the cleaned glass substrate at the spinning speed of 3000 rpm for 30 s. Then dried at 180 °C for 20 min and cooled naturally. This procedure was repeated five times. The final films were annealed at 500 °C for 2 h. The flow process for sol–gel spin coating mentioned in Fig. 1.

The crystal structure for all the thin films were analyzed by X-ray powder diffractometer (PANalytical—PW 340/60 X’pert PRO) with $\text{CuK}\alpha$ ($k = 1.5406 \text{ \AA}$). The CaMgZnO thin film surface morphology was observed using SEM (Model: Nova nanoSEM 450). The roughness was measured by the ellipsometer (J.A.Woollam co.M-2000U) and found 15.06, 22.9, 39.34, and 32.84 nm for sample 1, 2, 3, and 4 respectively. The optical properties were carried out by using Perkin Elmer double beam spectrophotometer (LAMBDA 35) in the UV–Vis–NIR region. The films thickness was measured by surface profilometer and found about 200 nm. The contact angle and freezing temperature were characterized by a DataPhysics OCA 20 instrument (DataPhysics GmbH, Germany). This system contains a high-speed CCD camera, a droplet-dispensing unit operate with a computer program and a peltier cooling stage. The results were evaluated by using SCA-20 software. The CaMgZnO samples were placed on cooling stage and dispensed a 4 μl droplet of water to measure contact angle and freezing temperature at about 25–30% humidity with around 22 °C room temperature.

3 Results and discussion

3.1 XRD analysis

The Fig. 2a showed the XRD spectrum regarding the calcium and magnesium co-doped ZnO (CaMgZnO) nano-films. It can be observed that all the samples had wurtzite-type structure. All the diffraction peaks were corresponding to zinc oxide (JCPDS card no. 36–1451). The XRD spectra of CaMgZnO samples 3 and sample 4 with calcium concentration of 2.5 and 4 at% showed peaks corresponding to (100), (002), and (101) planes. However, CaMgZnO samples 1 and sample 2 with 0 and 1% calcium only showed (002) plane. In all cases, (002) plane dominance was observed due to lowest surface free energy in c -axis direction [44]. Similar results for (002) dominance reported in the literature [20]. No other phases of impurity like MgO and CaO was observed. This could be due to the reason that Ca and Mg were successfully substituted into Zn site. Furthermore, hexagonal wurtzite structure was well-kept with magnesium and calcium concentration.

It can be noted that the intensity of the XRD peak reduced with the increment of Ca concentration. Also, the peak broadening can be observed with more calcium doping percentage. Moreover, the peak shift was observed as the calcium concentration increased. Since calcium with larger

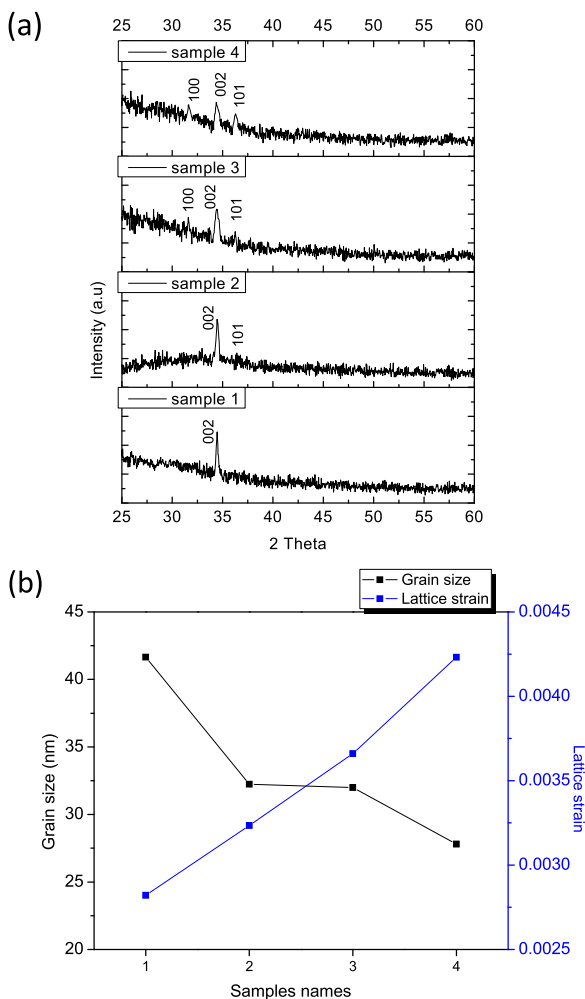


Fig. 2 **a** XRD spectra, **b** grain size and lattice strain variation, for calcium and magnesium co-doped ZnO thin film

Table 1 The grain size, lattice constants, lattice strain, dislocation density, and lattice ratio for CaMgZnO films

Sample	<i>D</i> (nm)	<i>a</i> (nm)	<i>c</i> (nm)	ϵ	Δ	<i>c/a</i>
1	41.66	0.3267	0.5204	0.002821	0.000576	1.592899
2	36.24	0.3267	0.5208	0.003235	0.000761	1.594123
3	32	0.3268	0.5211	0.003661	0.000977	1.594553
4	27.8	0.3267	0.5219	0.004231	0.001294	1.597490

ionic radius substitutes the Zn site and produces a shift to smaller angle [45]. The XRD diffraction peak positioned for (002) plane at 2θ angle as 34.47, 34.44, 34.41, and 34.36 for sample 1, sample 2, sample 3, and sample 4 respectively. The peak shift to smaller angles commonly credited to the increasing of the lattice constant [20]. Also, this is a common behavior due to substitution of larger ionic radius of calcium on Zn site. The similar results reported for larger ionic radius substitution in zinc site [46]. Our results

indicate that co-doped ZnO films can be prepared by sol–gel method without impurity phase.

The crystallite size, lattice constants, lattice strain, and dislocation density for CaMgZnO thin films showed in Table 1. The average crystallite size (*D*) was calculated for (002) preferred plane using the given scherrer's formula below [15].

$$D = \frac{k\lambda}{\beta \cos\theta} \quad (1)$$

Here *k* has the constant value of 0.9 and λ is the X-ray wavelength. The terms β and θ are the full width at half maximum and Bragg's angle of diffraction peak, respectively. The values of lattice strain and dislocation density were calculated by the formulas below [47]. These values were higher for sample 3 and sample 4 suggested that both were sensitive to co-doping. There was an inverse relation for grain size and lattice strain. The Fig. 2b plots explained the variation in lattice strain according to grain size difference by co-doping concentration.

$$\epsilon = \frac{\beta}{4 \tan\theta} \quad (2)$$

$$\delta = \frac{1}{D^2} \quad (3)$$

In the same way, lattice constants were calculated by the following formulae [48].

$$a = \frac{\lambda}{\sqrt{3} \sin\theta} \quad (4)$$

$$c = \frac{\lambda}{\sin\theta} \quad (5)$$

The tabular presentation of the above values showed in Table 1 below.

3.2 SEM and EDS analysis

The Fig. 3 presented the SEM images of different CaMgZnO samples. Figure 3a1, a2 showed sample 1 and its magnified image having 0% calcium and 2.5% Mg. It had closely packed uniformly distributed grains with relatively smooth surface. Figure 3b1, b2 presented the image for sample 2 and magnified result having 1% Ca and 2.5% Mg. It had agglomerate surface. Figure 3c1, c2 elucidated the picture and magnified result for sample 3 with 2.5% calcium concentration and 2.5% Mg content. This sample had wrinkles distributed on the entire surface. The sample 4 and its magnified image with 4% calcium doping level and 2.5% Mg content showed a dense wrinkled stressed type structure

Fig. 3 SEM images of calcium and magnesium co-doped ZnO thin film (a1)

Ca_{0.0}Mg_{0.025}Zn_{0.975}O

(sample 1) (a2) sample 1 magnified image, (b1)

Ca_{0.01}Mg_{0.025}Zn_{0.965}O

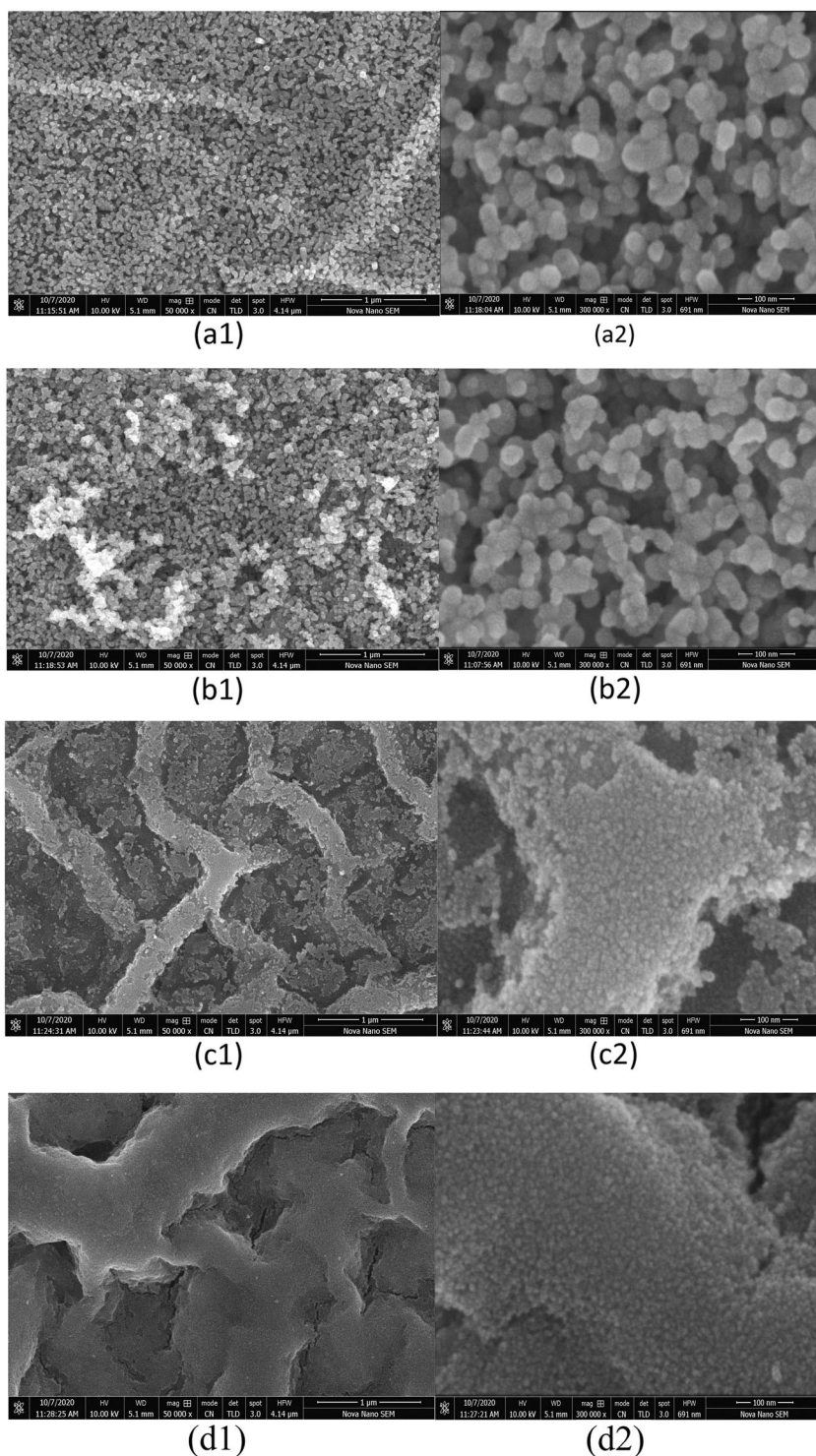
(sample 2) (b2) sample 2 magnified image, (c1)

Ca_{0.025}Mg_{0.025}Zn_{0.950}O

(sample 3) (c2) sample 3 magnified image, (d1)

Ca_{0.04}Mg_{0.025}Zn_{0.935}O

(sample 4) (d2) sample 4 magnified image



as presented in Fig. 3d1, d2. The nano-structure revealed that all the deposited films were crack free. It can be noted that as the calcium concentration increased the structure of the surface became wrinkled and stressed. It may be attributed to the difference of ionic radius of calcium with zinc and magnesium. Since zinc and magnesium has comparable ionic radius. Also, the smoother morphology of low

Ca concentration films was credited to the nucleation, growth, and activation energy relationship of thin films [49]. Furthermore, particle size reduced with the increment of calcium concentration.

The EDX spectra with weight % for CaMgZnO thin films showed in Fig. 4. The elements Zn, Mg, and Ca were present in the films and it elucidated that Mg and Ca

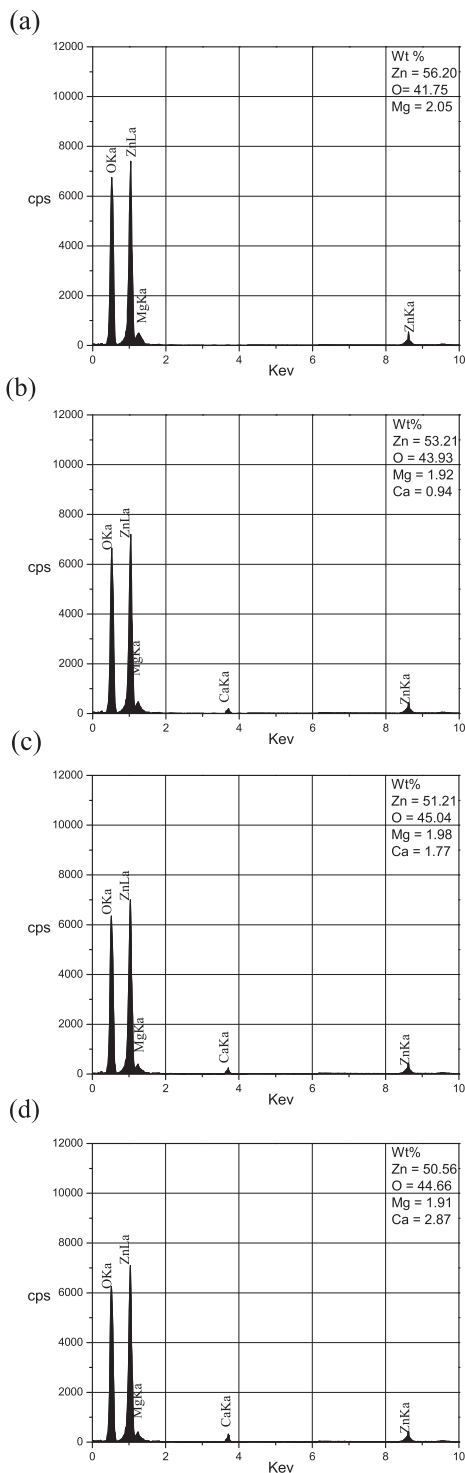


Fig. 4 EDS spectra for calcium and magnesium co-doped ZnO thin films **a** Ca_{0.0}Mg_{0.025}Zn_{0.975}O (sample 1), **b** Ca_{0.01}Mg_{0.025}Zn_{0.965}O (sample 2), **c** Ca_{0.025}Mg_{0.025}Zn_{0.950}O (sample 3), **d** Ca_{0.04}Mg_{0.025}Zn_{0.935}O (sample 4)

successfully substituted and replaced Zn in the host lattice. The magnesium was indicated by the peak near at 1.25 KeV. The zinc and oxygen detected by the peaks at

1.012 and 0.525 KeV, respectively. The peak at 3.72 KeV indicated the calcium presence.

3.3 UV-vis and optical analysis

The optical properties of calcium and magnesium co-doped zinc oxide were examined in the wavelength range of 300–800 nm. The Fig. 5 contained the detail of optical transmittance, absorbance and band gap for CaMgZnO films. From Fig. 5a the transmittance spectra showed obvious interference fringes in the visible region. The average transmittance for all the sample films was greater than 80% and represented a good optical quality. As the wavelength increased the transmittance had a fine absorption edge between 340 and 360 nm ranges. Furthermore, the sharp fall of the transmittance indicated a good crystal quality of all the deposited films. Similarly, Fig. 5b presented the absorbance spectra of all the CaMgZnO deposited films.

The value of direct band gap (E_g) was determined by the tauc's equation [44, 47]

$$\alpha(h\nu) = B(h\nu - E_g) \quad (6)$$

where ($h\nu$), α and B is the photon energy, absorption coefficient and constant respectively. To make a plot between $(\alpha h\nu)^2$ and $(h\nu)$ extrapolating the linear portion on $(h\nu)$ axis gives energy band gap.

The band gap for different Ca concentration in CaMgZnO films plotted in Fig. 5c. The band gap increment had been observed with the insertion of Ca as dopant. The band gap value for sample 1 with 0% calcium was 3.32 eV and close consistent with the reported result [15]. After increased Ca doping the band gap enhanced to 3.43 eV and indicated that the Ca ion entered into zinc oxide lattice as confirmed by our XRD result. This was due to the fact that Ca substituted Zn in ZnO lattice and produced defects due to the electronegativity and ionic radius difference between Ca and Zn, same was the case for Mg ion [44]. Since ZnO (3.20 eV) has lesser band gap compared to MgO [50]. As MgO and CaO have lower electron affinity than ZnO, the electron contribution positioned at higher Fermi level for CaMgZnO films. In consequence, the exciton recombination may produced the blue shift.

The other optical parameters to explore further the optical quality of the samples are optical constants (refractive index (n) and extinction coefficient (k)). These were estimated as a function of wavelength by the UV-vis spectroscopic records. The Fig. 6a, b depicted the graphical description of optical constants (n and k). The refractive index results ranged between 2.15 and 1.6 for all samples. The sample 1 and sample 2 obtained low refractive index and predicted less opaque nature as compared to rest of two

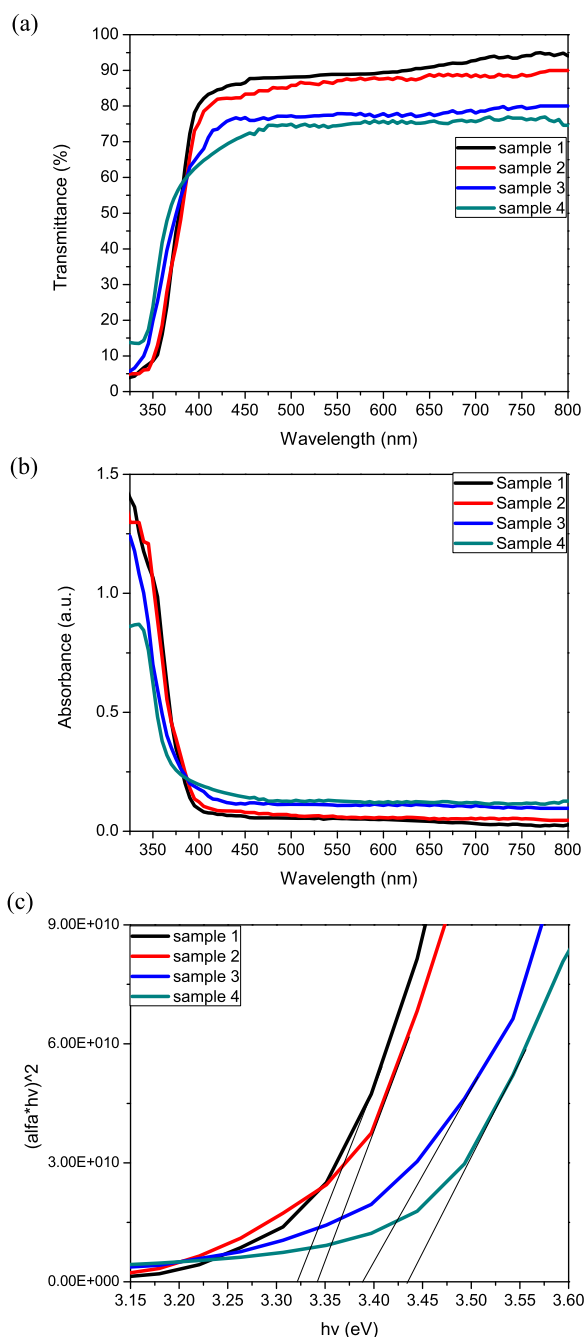


Fig. 5 UV–vis plots for calcium and magnesium co-doped ZnO thin film **a** transmittance, **b** absorbance, **c** band gap

due to plane surface and quality. Its value decreased as the wavelength changed. This credited to the reduction in optical absorption and consistent with UV–vis results (transmittance). On the contrary, the other samples having more overall impurity (doping species) produced more refractive index and extinction coefficient ascribed more optical absorption. In the same way, the extinction coefficient plotted in the visible region and values were in between 0.05 and 0.1. The high and incremented with

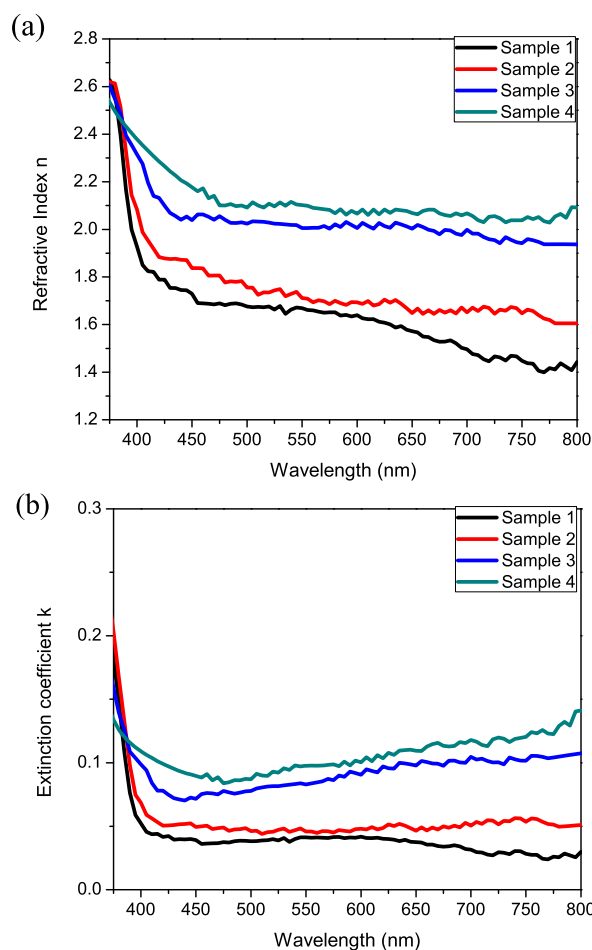


Fig. 6 Optical constants plots for calcium and magnesium co-doped ZnO thin film **a** n , **b** k

increased wavelength value of k for sample 3 and sample 4 was due to optical lose by low crystalline quality of the rougher surface [51, 52], as presented by the SEM images and less grain size by XRD data. Since greater grain size produced better transmittance [53]. The difference in the optical constant values for all the samples was due to surface morphology produced with variation of doping species. The comparable results were reported for doped ZnO [9, 51]. The optical constants were estimated by the following relations [9]

$$n = \left(\frac{1 + R}{1 - R} \right) + \left(\sqrt{\frac{4R}{(1 - R)^2} - k^2} \right) \tag{7}$$

$$k = \alpha\lambda/4\pi \tag{8}$$

The complex functions ϵ_r (real part) and ϵ_i (imaginary part) are called complex dielectric constants and gives the information related to the phonons excitation and optical

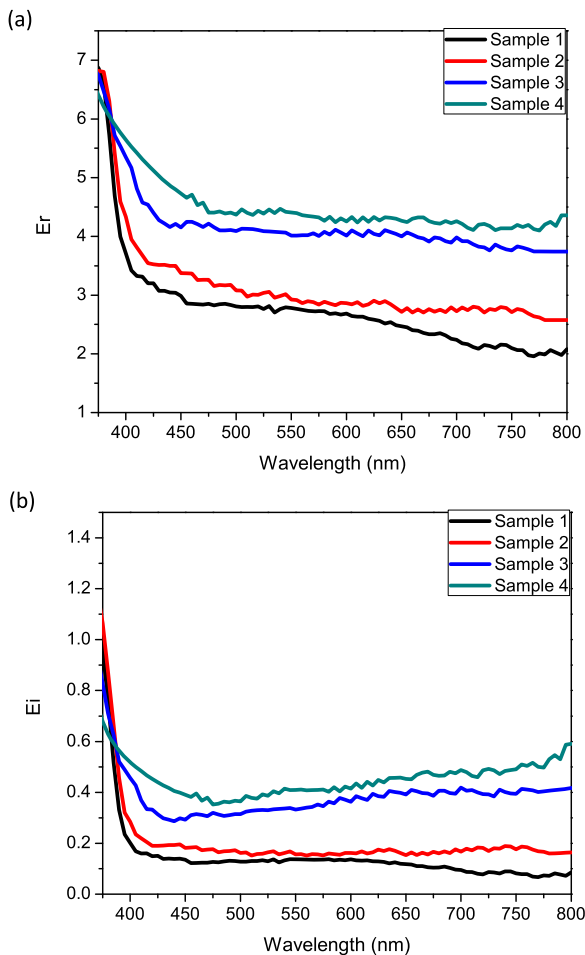


Fig. 7 Complex dielectric constant plots for Calcium and Magnesium co-doped ZnO thin film **a** ϵ_r , **b** ϵ_i

transition. These were calculated by the following relations [9, 52].

$$\begin{aligned}\epsilon &= \epsilon_r + \epsilon_i \\ \epsilon_r &= n^2 + k^2 \\ \epsilon_i &= 2nk\end{aligned}\quad (9)$$

The useful characteristic of optoelectronic devices is the polarization variation with photon energy. The information about the structure of a material can be collected by the electron excitation by photon energy. The electron excitation can be elaborated by the complex dielectric function. Figure 7a, b showed ϵ_r and ϵ_i lie in the range 2–7 and 0.1–1.5 respectively. These showed the better optical response compared to optical constants. The ϵ_r values were greater for sample 3 and sample 4 and that revealed more Ca with Mg in ZnO produced significant effects on optical properties. The ϵ_i values for sample 3 and sample 4 were more than other samples and suggested these samples contained more structural defects. In consequence of this, the previous optical results for these samples were also less

impressive except band gap. Therefore, the structure surface may be rougher compared to sample 1 and sample 2 as elucidated by the SEM results. The similar suggestions were as reported by Mohd shkir et al. [52]. Furthermore, the energy loss functions for volume and surface are volume energy loss function (VELF) and surface energy loss (SELF). These functions define the energy loss rate in a material for electron and related to ϵ_r and ϵ_i . The values for energy loss functions can be determined by the following relation [51, 52].

$$\text{VELF} = \epsilon_i / (\epsilon_r^2 + \epsilon_i^2) \quad (10)$$

$$\text{SELF} = \epsilon_i / ((\epsilon_r + 1)^2 + \epsilon_i^2) \quad (11)$$

The VELF and SELF spectra of CaMgZnO nano-films showed in Fig. 8a, b. Both plots of VELF and SELF were alike and indicated that the radiation crossing from upper and inner layer were similar. Also, SELF results were lesser compared to VELF. Therefore, more energy loss occurred by electronic transitions in the interior of CaMgZnO films. Moreover, the values for sample 3 and sample 4 were higher than others and close comparable. This indicated structural disorder and may be rougher surface.

Another optical parameter is known as optical conductivity (σ). This explains the enriched response w.r.t photon energy ($h\nu$). The results for σ were calculated by the relation $\sigma = \omega n c / 4\pi$ [9], here c is the speed of light. The Fig. 8c presented the value of σ . This showed that optical conductivity increased with increment of photon energy may be because of electron excitement through photon energy. The σ values shifted to higher energy from sample 1 to sample 4 due to conductivity at higher energy by structural defects. This proved higher band gap as also confirmed by τ_{auc} 's plot. Similar findings reported for different materials [9, 54, 55].

3.4 Photoluminescence (PL) analysis

The results for the luminescence properties of CaMgZnO films presented in Fig. 9. The PL analysis plays an important role to probe quality of the material and defect density. All the deposited CaMgZnO films exhibited two main peaks. The first one located near the UV region between wavelength 300–400 nm and the second one between 450–750 nm in the visible region. These two emissions explain the quality of the crystal (UV) and structural defects (visible) for the deposited films [56]. The intensity of UV peak decreased as the Ca concentration increased and indicated minor quality (defect center increment) deteriorated. Since higher ionic radii of Ca (0.99 \AA) than Zn (0.74 \AA) and Mg (0.57 \AA), caused distortion in zinc oxide structure and increased defects in material. Furthermore, the peak shifted to lower wavelength with Ca addition

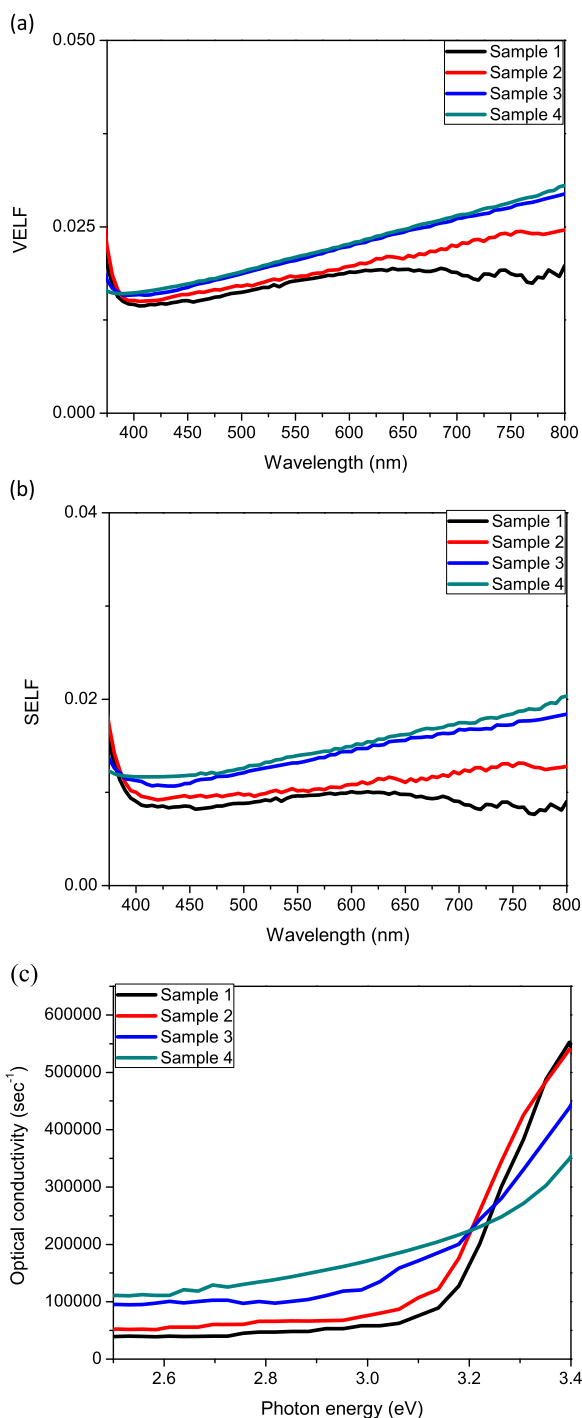


Fig. 8 Energy loss functions and optical conductivity plots for Calcium and Magnesium co-doped ZnO thin film **a** VELF, **b** SELF, **c** σ

considered band gap increment [57]. The PL intensity of UV peak found for sample 4 was around 360 nm (3.43 eV) which is in good agreement with UV–vis result. In general, the visible emission originated from the defects including zinc, oxygen vacancies, and interstitials [58]. The UV band related to the free excitons recombination by exciton–exciton collision [59]. The ratio of UV–visible

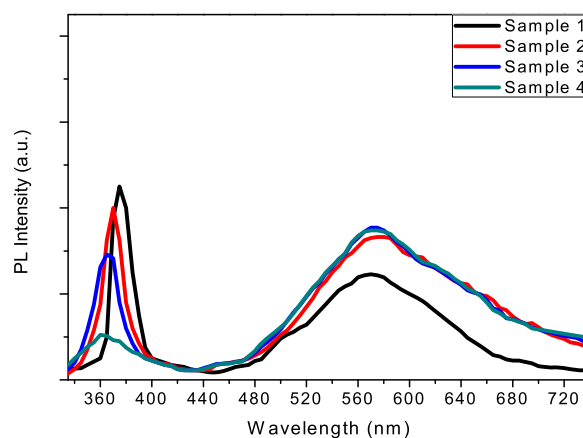


Fig. 9 PL spectra of calcium and magnesium co-doped ZnO thin films

emissions intensities for all the samples considered to be good optical and crystal quality for CaMgZnO samples.

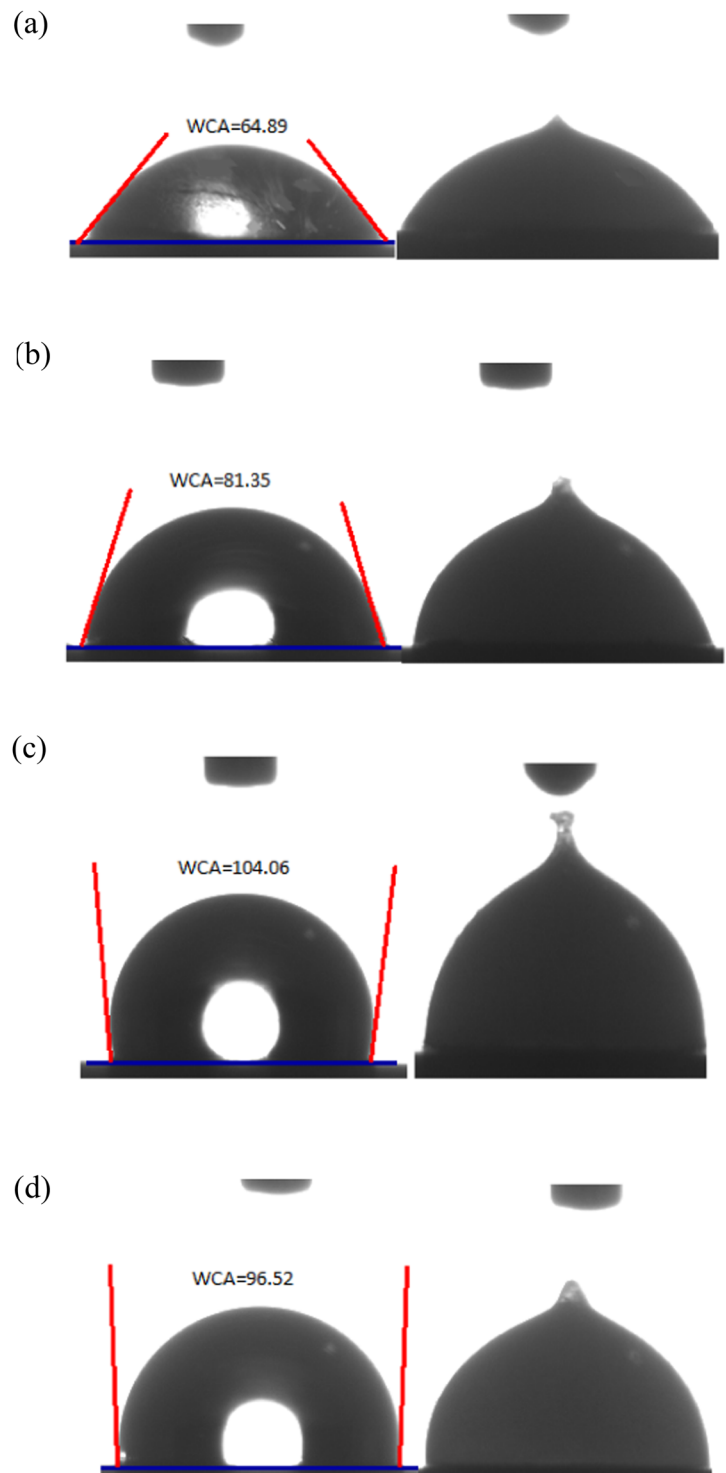
3.5 Contact angle and freezing analysis

The water contact angle (WCA) and freezing results were taken by depositing 4 μ l water droplet on the surface of all the samples. The contact angle (θ) of a droplet can be measured conventionally at a liquid–vapor interface on a solid surface. The theoretical calculation of contact angle can be estimated by the Young–Dupre formula [8].

$$\cos \theta = (\gamma_{sv} - \gamma_{sl}) / \gamma_{lv} \quad (12)$$

Here γ is the surface tension for solid–vapor, solid–liquid, and liquid–vapor interface. Figure 10 showed the images of water droplet for all CaMgZnO samples. The left side of figure showed droplets of water at room temperature. For the sample 1 and sample 2, the surface looked hydrophilic because the contact angle was lesser than 90 degree [60]. While the other sample 3 and sample 4 were hydrophobic as their contact angle was $>90^\circ$. The hydrophobic behavior increased with more calcium concentration. The raised contact angle for sample 3 and sample 4 may be attributed to the reduction in surface energy by structural change due to calcium concentration [61]. Moreover, the variation in contact angle can be attributed to microstructural changes with doping variation [46]. The right side of Fig. 10 showed the image of water droplet after freezing. During the cooling stage, the temperature of the water surface decreased and nucleation of ice occurred by sufficient super-cooling. The report [62] on water cooling explains that freezing has two stages (i) recalescence stage is a short period stage during which a slushy mixture of ice and water occurs, (ii) second is the isothermal freezing of the remaining liquid. Freezing on-set temperature for all the samples was determined at the point just before when the appearance of droplet changed

Fig. 10 Water droplet contact angle and freeze images for calcium and magnesium co-doped ZnO thin film **a** sample 1, **b** sample 2, **c** sample 3, **d** sample 4



from optically light to dark and the cooling rate was $5\text{ }^{\circ}\text{C}/\text{min}$. This temperature varied as $-8.1\text{ }^{\circ}\text{C}$, $-9.6\text{ }^{\circ}\text{C}$, $-15.1\text{ }^{\circ}\text{C}$, $-13.9\text{ }^{\circ}\text{C}$ for the sample 1, sample 2, sample 3, and sample 4 respectively. Comparison plot between contact angle of water droplet and freezing on-set temperature with error (at least three readings) presented in Fig. 11b. Most improved measurements found for sample

3 with less error. Similar and opposite results of contact angle for co-doped ZnO by chemical method were reported in literature [8, 46].

Figure 11a depicted the plots of contact angle measurement as a function of temperature for finest measurement. The drop and variation in the contact angle especially after $0\text{ }^{\circ}\text{C}$ attributed to the frost formation that made the sample

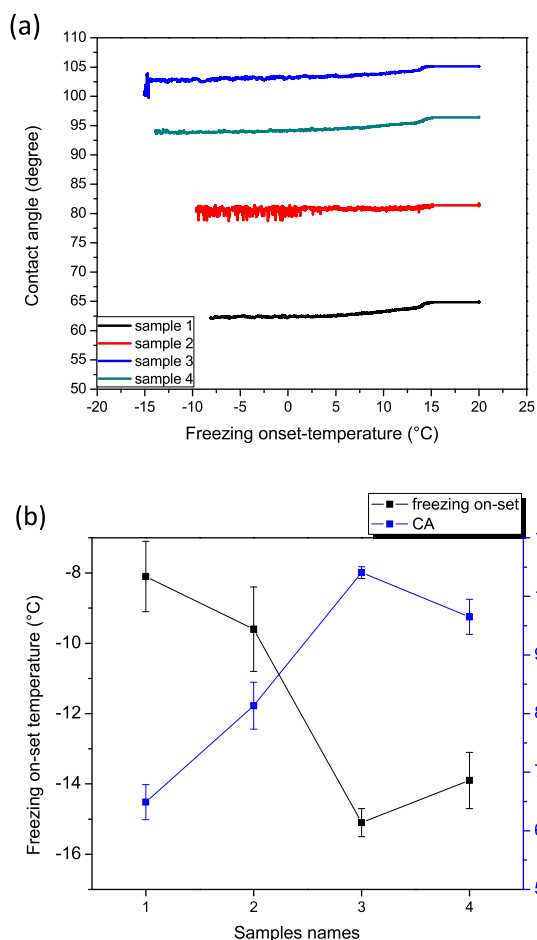


Fig. 11 **a** Water droplet contact angle as a function of temperature for calcium and magnesium co-doped ZnO thin film, **b** comparative plot of contact angle with freezing on-set temperature

surface hydrophilic as reported the same suggestion for sapphire sample [62].

Time measured after a temperature set-point up to water droplet freezing is called freezing delay. To measure freezing delay, an experiment was done by placing water droplets on all samples separately and at least three readings were taken to find error. After that the samples were cooled down slowly at the rate of 5 °C/min to the set points of −5 and −10 °C individually. The results of all samples for freezing delay offered in Fig. 12. The maximum freezing delay time measured for the sample 3 with less error. The results for freezing delay of sample 3 were 900 and 630 s for −5 and −10 °C set-point, respectively. Since sample 3 had equal amount of doping species (Ca, Mg) and best result given by this sample may be attributed to equal roughness distributed on the entire surface. As the roughness is the key factor to control ice formation (ice-phobicity) as reported in the literature [38–41]. The detail regarding different findings for all the samples presented in Table 2.

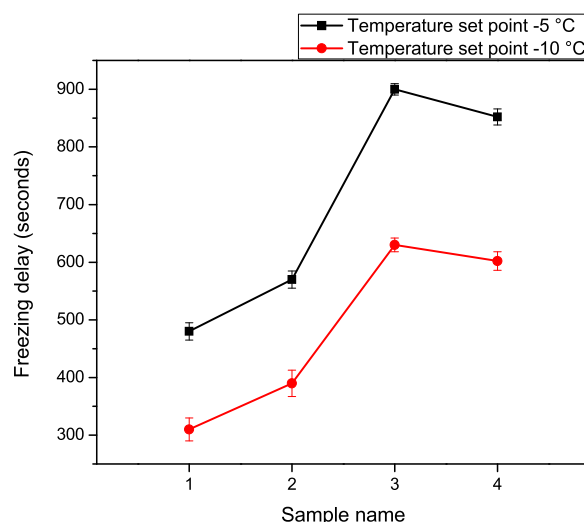


Fig. 12 Freezing delay plot for calcium and magnesium co-doped ZnO thin film with set-point −5 and −10 °C

Ice-phobic surface defined generally as very surface that can avoid ice formation under freezing conditions. For de-icing properties, the two main parameters are wettability and roughness [63]. Alizadeh et al. [64] prepared hydrophobic surface and used for delay in ice nucleation. The ice nucleation rate on hydrophobic surface compared to hydrophilic was delayed 80 s for −20 °C. Li et al. [65] compared the freezing state on two different surfaces having different wettability of 55.2° and 113.7°. The result revealed that ice nucleation rate was low with higher contact angle. Boinovich et al. [66] fabricated hydrophobic surface by using pulsed laser method to create a multi surface roughness required for super-hydrophobicity. They investigated freezing delay at −20 °C to around 6 h with super-hydrophobicity of 172.5° WCA. He et al. [67] reported ice nucleation on the super-hydrophobic surface was slower than the ice formation on the hydrophilic surface. Yang and Li [68] explored that super-hydrophobic surface produced more icing delay of 12 min than hydrophobic. Liu et al. [69] studied the icing delay time of super-hydrophobic surface was 55 min at −10.1 °C compared to hydrophilic surface. Kulinich and Farzaneh [70] investigated that rougher super-hydrophobic (150° CA) surface created low ice adhesion than hydrophobic (120° CA) coating. Qitao et al. [38] prepared two groups of sol-gel coating samples having different surface roughness and energy. They examined that low surface energy and roughness coatings were ice-phobic. Since low surface energy produces higher contact angle. Similar findings reported in literature regarding surface roughness as [39].

All this indicated that surface structure (smooth roughness) and contact angle influences ice accumulation. The smooth rougher with less contact area of surface to water droplet enhances the delay in ice formation by the slow

Table 2 The transmittance, band gap, refractive index, contact angle, freezing on-set temperature and freezing delay for CaMgZnO films

Sample	Transmittance (%)	Band gap (eV)	Refractive index	Wetting (CA) (degrees)	Freezing on-set (°C)	Freezing delay (seconds) set-point –5 °C	Freezing delay (seconds) set-point –10 °C
1	92	3.32	1.6	64.89	–8.1	480	310
2	87	3.34	1.8	81.35	–9.6	570	390
3	79	3.39	2.05	104.06	–15.1	900	630
4	75	3.43	2.15	96.52	–13.9	852	602

transfer of energy from cold surface to droplet. In our case, the sample 3 had small grain and particle size as revealed by XRD and SEM results with more roughness (ellipsometer 39.34 nm) compared to others, tended to delay in ice accumulation attributed to less contact area from surface to water droplet and proportionally less energy transfer from surface. The hydrophobic surface and coatings can be beneficial for anti-icing and self-cleaning [71], anti-fouling [72], anti-fogging [73], and anti-corrosion surfaces [74]. Another reason for selection of hydrophobic surface as ice-phobic surface is that this surface tends to reduce the quantity of water droplets on the surface and runs off by rolling before freezing [75, 76].

4 Conclusion

The calcium and magnesium co-doped ZnO (CaMgZnO) thin films were well synthesized on glass substrate by sol–gel spin coating technique. Various properties of CaMgZnO films were investigated as a function of different calcium doping concentrations. The XRD and SEM results exhibited *c*-axis preferred morphology and showed crack free surface respectively. The band gap values varied from 3.32 to 3.43 eV from single magnesium doping to co-doping with 4 at% maximum calcium respectively. All the films were maximum transparent in the range from 90 to 70% in visible region. Optical constants presented the results that indicated low transparency and optical loss for concentrated doped samples. Complex dielectric constants and energy loss functions also supported the optical constants analysis and revealed the structural disorder. Optical conductivity proved the band gap enhancement with doping concentration. Furthermore, photoluminescence study also revealed the structural deterioration with the addition of doping concentration by UV and visible intensity difference. The water contact angle results revealed the hydrophobic behavior of sample having more dopants. The hydrophobicity proved by the 104.06° CA and this behavior remained throughout freezing process, also freezing on-set was –15.1 °C related to this CA. Maximum freezing delay produced by the sample with equal amount of Ca and Mg

concentration and verified its smooth roughness (39.34 nm) as compared to other samples. Freezing delay time was observed as 900 s and 630 s for –5 and –10 °C set-point respectively. Therefore, the co-doping of calcium with magnesium in ZnO may be useful for application concerning with hydrophobicity like self-cleaning. Also, finding results proved that prepared films with a low-cost sol–gel method can be suitable for applications regarding anti-icing behavior.

Acknowledgements The authors would like thanks to Head of Physics Department and Nano Electronics Research lab, GC University Lahore. FB would like thanks to HEC Pakistan for IRSIP scholarship to conduct research in University of Bergen Norway. He also acknowledges the Head of Nano-Physics group Department of Physics and Technology, University of Bergen Norway.

Compliance with ethical standards

Conflict of interest The authors declare that they have no conflict of interest.

Publisher's note Springer Nature remains neutral with regard to jurisdictional claims in published maps and institutional affiliations.

References

1. Wang J, Han F, Liang B, Geng G (2017) Hydrothermal fabrication of robustly superhydrophobic cotton fibers for efficient separation of oil/water mixtures and oil-in-water emulsions. *J Ind Eng Chem* 54:174–183
2. Wang L, Gong Q, Zhan S, Jiang L, Zheng Y (2016) *Adv Mater* 28:7729
3. Kang Z, Li W (2017) Facile and fast fabrication of superhydrophobic surface on magnesium alloy by one-step electrodeposition method. *J Ind Eng Chem* 50:50–56
4. Boreyko J, Chen CH (2009) Self-Propelled dropwise condensate on superhydrophobic surfaces. *Phys Rev Lett* 103:184501
5. Chu F, Wu X, Zhu B, Zhang X (2016) Self-propelled droplet behavior during condensation on superhydrophobic surface. *Appl Phys Lett* 108:194103
6. Li W, Kong C, Qin G, Ruan H, Fang L (2014) p-Type conductivity and stability of AgeN codoped ZnO thin films. *J Alloy Compd* 609:173–177
7. Souissi R, Mimouni M, Amlouk S (2015) Guermazi, SiO₂ substrate and Mo, In codoping effect on crystalline and vibrational

- characteristics of ZnO sprayed thin films. *Superlattices Microstruct* 85:707–715
8. Mimouni R, Mahdhi N, Boubaker K, Madouri A, Amlouk M (2016) Physical study on cobalt-indium co-doped ZnO nanofilms as hydrophobic surfaces. *Superlattices Microstructures* 91:345–357
 9. Fermi Hilbert Inbaraj P, Joseph Prince J (2018) Optical and structural properties of Mg doped ZnO thin film by chemical bath deposition method. *J Mater Sci Mater Electron* 29:935–943
 10. Srivastava A, Kumar N, Misra KP, Khare S (2014) Blue-light luminescence enhancement and increased band gap from calcium-doped zinc oxide nanoparticle films. *Mater Sci Semicond Process* 26:259–266
 11. Karthick K, Vijayalakshmi K (2014) Influence of Mg doping on the properties of ZnO films prepared on c-cut sapphire by sputtering. *Super Lattice Microstruct* 67:172–180
 12. Chen H, Ding J, Ma S (2010) Structural and optical properties of ZnO:Mg thin films grown under different oxygen partial pressure. *Phys E* 42:1487–1491
 13. Madahi P, Shahtahmasebi N, Kompany A, Mashreghi M, Bagheri-Mohagheghi MM, Hosseini A (2011) Deposition and characterization of ZnO:Mg thin films: the study of antibacterial properties. *Phys Scr* 84:035801
 14. Vijayalakshmi K, Renitta A, Karthick K (2014) Growth of high quality ZnO:Mg films on ITO coated glass substrates for enhanced H₂ sensing. *Ceram Int* 40:6171–6177
 15. Mia MNH, Pervez MF, Khalid Hossain M, Reefaz Rahman M, Jalaludin M, Almashud MA, Ghosh HK (2017) Mahbulul Haq, Influence of Mg content on tailoring optical bandgap of Mg doped ZnO thin film prepared by sol-gel method. *Results Phys* 7:2683–2691
 16. Caglar M, Caglar Y, Ilican S (2016) Investigation of the effect of Mg doping for improvement of optical and electrical properties. *Phys B* 485:6–13
 17. Huang K, Tang Z, Zhang L, Yu J, Lv J, Liu X, Liu F (2012) Preparation and characterization of Mg doped ZnO thin films by sol-gel method. *Appl Surf Sci* 258:3710–3713
 18. Hussain KA, Aadim HM (2014) Slman, Structural and optical properties of Mg doped ZnO thin films deposited by pulse laser deposition (PLD), Iraq. *J Phys* 12:56–61
 19. Verma K, Chaudhary B, Kumar V, Sharma V, Kumar M (2017) Investigation of structural, morphological and optical properties of Mg:ZnO thin films prepared by sol-gel spin coating method. *Vacuum* 146:524–529
 20. Anca-Ionela I, Florin N, Iuliana M, Florin C, Raluca G, Oana T, Cosmin R, Vasilica T, Nedelcu M, Müller R (2019) Synthesis and characterization of Ca doped ZnO thin films by sol-gel method. *J Sol-Gel Sci Technol* 92:585–597
 21. Mondal C, Ganguly M, Sinha AK, Pal J, Pal T (2013) Fabrication of a ZnO nanocolumnar thin film on a glass slide and its reversible switching from a superhydrophobic to a superhydrophilic state. *RSC Adv* 3:5937e5944
 22. Yan B, Tao J, Pang C, Zheng Z, Shen Z, Huan CHA, Yu T (2008) Reversible UV-light-induced ultrahydrophobic-to-ultrahydrophilic transition in an a-Fe₂O₃ nanoflakes film. *Langmuir* 24:10569–10571
 23. Sinha AK, Basu M, Pradhan M, Sarkar S, Negishi Y, Pal T (2011) Redox-switchable superhydrophobic silver composite. *Langmuir* 27:11629–11635
 24. Chaudhary G, Li R (2014) Freezing of water droplets on solid surfaces: an Experimental and Numerical Study. *Exp Therm Fluid Sci* 57:86–93
 25. Lv J, Song Y, Jiang L, Wang J (2014) Bio-Inspired Strategies for Anti-Icing. *ACS Nano* 8:3152–3169
 26. Chen J, Liu J, He M, Li K, Cui D, Zhang Q, Zeng X, Zhang Y, Wang J, Song Y (2012) Superhydrophobic surfaces cannot reduce ice adhesion. *Appl Phys Lett* 101:111603
 27. Graeber G, Schutzius TM, Eghlidi H, Poulikakos D (2017) Spontaneous self-dislodging of freezing water droplets and the role of wettability. *Proc Natl Acad Sci* 114:11040–11045
 28. Meuler J, McKinley GH, Cohen RE (2010) Exploiting topographical texture to impart icephobicity. *ACS Nano* 4:7048–7052
 29. Laforte JL, Allaire MA, Laflamme J (1998) State-of-the-art on power line de-icing. *Atmos Res* 46:143–158
 30. Jung S, Dorrestijn M, Raps D, Das A, Megaridis CM, Poulikakos D (2011) A resuper hydrophobic surfaces best for icephobicity? *Langmuir* 27:3059–3066
 31. Zhang S, Huang J, Cheng Y, Yang H, Chen Z, Lai Y (2017) Bio inspired surfaces with superwettability for anti-icing and ice-phobic application: concept, mechanism, and design. *Small* 13:1–20.
 32. Jellinek HH (1959) Adhesive properties of ice. *J Colloid Sci* 14:268–280
 33. Raraty LE, Tabor D (1958) The adhesion and strength properties of ice. *Proc R Soc A Math Phys Eng Sci* 245:184–201
 34. Schutzius TM, Jung S, Maitra T, Eberle P, Antonini C, Stamatopoulos C, Poulikakos D (2015) Physics of icing and rational design of surfaces with extraordinary icephobicity. *Langmuir* 31:4807–4821
 35. Lv J, Song Y, Jiang L, Wang J (2014) Bio-inspired strategies for anti-icing. *ACS Nano* 8:3152–3169
 36. Kreder MJ, Alvarenga J, Kim P, Aizenberg J (2016) Design of anti-icing surfaces: smooth, textured or slippery? *Nat Rev Mater* 1:15003
 37. Amin-Sarshar M, Song D, Swartz CH, Lee J, Choi CH (2018) Anti-icing or deicing: icephobicities of superhydrophobic surfaces with hierarchical structures. *Langmuir* 34:13821
 38. Fu Q, Wu X, Kumar D, Jeffrey WCHO, Kanhere PD, Srikanth N, Liu E, Wilson P, Chen Z (2014) Development of sol-gel icephobic coatings: effect of surface roughness and surface energy. *Appl Mater Interfaces* 6:20685–20692
 39. Fu QT, Liu EJ, Wilson P, Chen Z (2015) Ice nucleation behaviour on sol-gel coatings with different surface energy and roughness. *Phys Chem Chem Phys* 17:21492–21500
 40. Eberle P, Tiwari MK, Maitra T, Poulikakos D (2014) Rational nanostructuring of surfaces for extraordinary icephobicity. *Nanoscale* 6:4874–4881
 41. Wang S, Liu K, Yao X, Jiang L (2015) Bioinspired surfaces with superwettability: new insight on theory, design, and applications. *Chem Rev* 115:8230–8293
 42. Qi L, Zhiguang G (2018) Fundamentals of icing and common strategies for designing biomimetic anti-icing surfaces. *J Mater Chem A* 6:13549–13581
 43. Foo KL, Kashif M, Hashim U, Wei-wen L (2014) Effect of different solvents on the structural and optical properties of zinc oxide thin films for optoelectronic applications. *Ceram Int* 40:753–761
 44. Karzazi O, Soussi L, Louardi A, El Bachiri A, Khaider M, Monkade M, Erguig H, Taleb M (2019) Transparent conducting properties of Mg and Al co-doped ZnO thin films deposited by spray pyrolysis technique. *Superlattice Microstruct* 127:61–65
 45. Slama R, El Ghoul J, Omri K, Houas A, El Mir L, Launay F (2016) Effect of Ca-doping on microstructure and photocatalytic activity of ZnO nanoparticles synthesized by sol gel method. *J Mater Sci Mater Electron* 27:7939–7946
 46. Mohamed S, Sayed AMEI (2016) Effects of lanthanum and sodium on the structural, optical and hydrophilic properties of sol-gel derived ZnO films: a comparative study *Mater Sci Semiconduct Process* 41:323–334

47. Kumar KDA, Ganesh V, Shkir M, AlFaify S, Valanarasu S (2018) Effect of different solvents on the key structural, optical and electronic properties of sol-gel dip coated AZO nanostructured thin films for optoelectronic applications. *J Mater Sci Mater Electron* 29:887–897
48. Bekkari R, Jaber B, Labrim H, Ouafi M, Zayyoun N, Laanab L (2019) Effect of solvents and stabilizer molar ratio on the growth orientation of sol-gel derived ZnO thin films. *Hindawi Int J Photoenergy* 3164043:7
49. Kim I, Shin SW, Gang MG, Leea SH, Gurav KV, Patil PS, HoYun J, Lee JY, Kim JH (2014) Comparative study of quaternary Mg and group III element co-doped ZnO thin films with transparent conductive characteristics. *Thin Solid Films* 570:321–325
50. Zhuang H, Wang J, Liu H, Li J, Xu P (2011) Structural and optical properties of ZnO nanowires doped with magnesium. *Acta Phys Pol A* 119:819–823
51. Baig F, Asif A, Muhammad Waseem A, Muhammad I (2020) Comparative study for seed layer solvent effects on structural and optical properties of MgZnO thin films deposited by chemical bath deposition technique *Mater Res Express* 7:026417
52. Shkir M, Arif M, Ganesh V, Manthrammel MA, Singh A, Yahia IS, Maidur SR, Patil PS, AlFaify S (2018) Investigation on structural, linear, nonlinear and optical limiting properties of sol-gel derived nanocrystalline Mg doped ZnO thin film for optoelectronic applications. *J Mol Struct* 1173:375–384
53. Lee JH, Ko KH, Park BO (2003) Electrical and optical properties of ZnO transparent conduction film by the sol-gel method. *J Cryst Growth* 247:119–125
54. Wakkad MM, Shokr EK, Mohamed SH (2000) Optical and calorimetric studies of Ge-Sb-Se glasses. *J Non-Cryst Solids* 265:157–166
55. El-Nahass MM, Soliman HS, Hendi AA, El-Gamdy SH (2011) *Aust J Basic Appl Sci* 5:145
56. Kashif M, Usman Ali SM, Ali ME, Abdulgafour HI, Hashim U, Willander M, Hassan Z (2012) Morphological, optical and raman characteristics of ZnO nanoflakes prepared via a sol-gel method. *Phys. Status. Solidi A* 209:143–147
57. Lee CT (2010) Fabrication methods and luminescent properties of ZnO materials for light emitting diode. *Materials* 3:2218–2259
58. Kashif M, Hashim U, Ali ME, Ali SMU, Rusop M, Ibupoto ZH, Willander M (2012) Effect of different seed solutions on the morphology and electrooptical properties of ZnO nanorods. *J Nanomater* 452407
59. Kai LF, Hashim U, Muhammad K, Voon CH (2014) Sol-gel synthesized zinc oxide nanorods and their structural and optical investigation for optoelectronic applications. *Nanoscale Res Lett* 9:429
60. Akhtar N, Holm VR, Thomas PJ, Svardal B, Askeland SH, Holst B (2015) Underwater superoleophobic sapphire (0001) surfaces. *J Phys Chem C* 119:15333–15338
61. Taherian F, Marcon V, van der Vegt NF, Leroy F (2013) What is the contact angle of water on graphene? *Langmuir* 29:1457–1465
62. Akhtar N, Anemone G, Farias D, Holst B (2019) Fluorinated graphene provides long lasting ice inhibition in high humidity. *Carbon* 141:451–456
63. Bharathidasan T et al. (2014) Effect of wettability and surface roughness on iceadhesion strength of hydrophilic, hydrophobic and superhydrophobic surfaces. *Appl Surf Sci* 314:241–250
64. Alizadeh A et al. (2012) Dynamics of ice nucleation on water repellent surfaces. *Langmuir* 28:3180–3186
65. Li K et al. (2012) Investigating the effects of solid surfaces on ice nucleation. *Langmuir* 28:10751–10753
66. Boinovich LB et al. (2016) Anti-icing properties of a superhydrophobic surface in a salt environment: an unexpected increase in freezing delay times for weak brine droplets. *Phys Chem Chem Phys* 18:3131–3136
67. He M et al. (2010) Super-hydrophobic film retards frost formation. *Soft Matter* 6:2396
68. Yang J, Li W (2013) Preparation of superhydrophobic surfaces on Al substrates and the anti-icing behavior. *J Alloy Compd* 576:215–219
69. Liu Z et al. (2008) Frost formation on a super-hydrophobic surface under natural convection conditions. *Int J Heat Mass Transf* 51:5975–5982
70. Kulinich SA, Farzaneh M (2009) Ice adhesion on superhydrophobic surfaces. *Appl Surf Sci* 255:8153–8157
71. Zhang X et al. (2013) Self-cleaning superhydrophobic surface based on titanium dioxide nanowires combined with polydimethylsiloxane. *Appl Surf Sci* 284:319–323
72. Bixler GD et al. (2014) Anti-fouling properties of microstructured surfaces bioinspired by rice leaves and butterfly wings. *J Colloid Interface Sci* 419:114–133
73. Chen Y et al. (2012) Transparent superhydrophobic/superhydrophilic coatings for self-cleaning and anti-fogging. *Appl Phys Lett* 101:033701
74. Chang KC et al. (2013) Nanocasting technique to prepare lotus-leaf-like superhydrophobic electroactive polyimide as advanced anticorrosive coatings. *ACS Appl Mater Interfaces* 5:1460–1467
75. Mishchenko L et al. (2010) Design of ice-free nanostructured surfaces based on repulsion of impacting water droplets. *ACS Nano* 4:7699–7707
76. Antonini C et al. (2011) Understanding the effect of superhydrophobic coatings on energy reduction in anti-icing systems. *Cold Reg Sci Technol* 67:58–67